

On rebuilding landslide parameters from long-period seismic waveform inversion

Xiao Wang¹, Xinghui Huang¹, Po Chen², Lei Xu³, Heng Wang², Wenze Deng¹, Dan Yu¹, Zhengyuan Li¹, and Qiang Xu⁴

¹China Earthquake Networks Center

²University of Wyoming

³The 7th Institute of Geology & Mineral Exploration of Shandong Province

⁴State Key Laboratory of Geo-Hazard Prevention and Geo-Environment Protection, Chengdu

November 22, 2022

Abstract

Landslide force history inverted from long-period seismic records for a landslide has been used to extract its physical parameters. An important precondition is that the inverted landslide force histories are reasonable approximations. We first discuss how to estimate the accuracy of the inverted force histories and then propose an approach to determine the proper frequency band used in the inversion. We perform a long-period seismic waveform inversion for the 2003 Qianjiangping landslide to obtain its force-time history and estimate its movement parameters. Based on the results, we build a simple model to study the effects of the portion of the initial sliding mass and the location of the mass entrainment on the seismically estimated mass, which shows that if the entrainment occurs at the slow-down phase the seismically estimated mass is a closer approximation of the initial sliding mass.

27 **Abstract**

28 Landslide force history inverted from long-period seismic records for a landslide has
29 been used to extract its physical parameters. An important precondition is that the
30 inverted landslide force histories are reasonable approximations. We first discuss how
31 to estimate the accuracy of the inverted force histories and then propose an approach
32 to determine the proper frequency band used in the inversion. We perform a
33 long-period seismic waveform inversion for the 2003 Qianjiangping landslide to
34 obtain its force time history and estimate its movement parameters. Based on the
35 results, we build a simple model to study the effects of the portion of the initial sliding
36 mass and the location of the mass entrainment on the seismically estimated mass,
37 which shows that if the entrainment occurs at the slow-down phase the seismically
38 estimated mass is a closer approximation of the initial sliding mass.

39 **Plain Language Summary**

40 A landslide is a dynamic process that occurs on the surface of the earth. The force
41 exerted on the earth's crust during the occurrence is propagated in the form of seismic
42 waves and recorded by the seismic station, which can be used to estimate the
43 kinematics and dynamics of the landslide. The difference of the parameters used in
44 obtaining the force sequence leads to different results for the same event, and the
45 understanding and interpretation of the event are also affected. In this study, we
46 discussed what kind of results are relatively reasonable and how to choose parameters
47 to get them. Besides, the driving force of the initial sliding is gravity, which can be
48 monitored by the earth's crust; during the sliding, the driving force of the passively
49 moving material is from the material that is already in motion, and this force cannot
50 be detected. We used a simple model to show the effect on the inversion results when
51 the mobilized material is located at different positions on the sliding path. The
52 simulation shows that if the material is entrained at the slow-down phase, the
53 seismically estimated mass is closer to the initial sliding mass.

54

55

56 1. Introduction

57 Landslide force history inversion using long-period seismic records based on a
58 Single-Force source model [e.g., *Dahlen, 1993; Fukao, 1995; Hasegawa and*
59 *Kanamori, 1987; Kanamori and Given, 1982; Kanamori et al., 1984*] and a fixed
60 point source assumption has been widely adopted to study landslide kinematics [e.g.,
61 *Allstadt, 2013; Ekström and Stark, 2013; Gualtieri and Ekström, 2018; Hibert et al.,*
62 *2014; Hibert et al., 2015; W Li et al., 2019; Moore et al., 2017; Moretti et al., 2015;*
63 *Sheng et al., 2020; Yamada et al., 2013; Zhao et al., 2020*]. The algorithms used in
64 previous studies, although not exactly the same in detail due to implementation
65 strategies by individual researchers, are proven to be robust. The authors of the
66 present study have also developed an algorithm to invert for landslide force histories
67 and have successfully applied it to the Wulong landslide [*Li et al., 2017*], the Xinmo
68 landslide [*Z-y Li et al., 2019*], and the Xiaoba landslide [*Yu et al., 2020*].

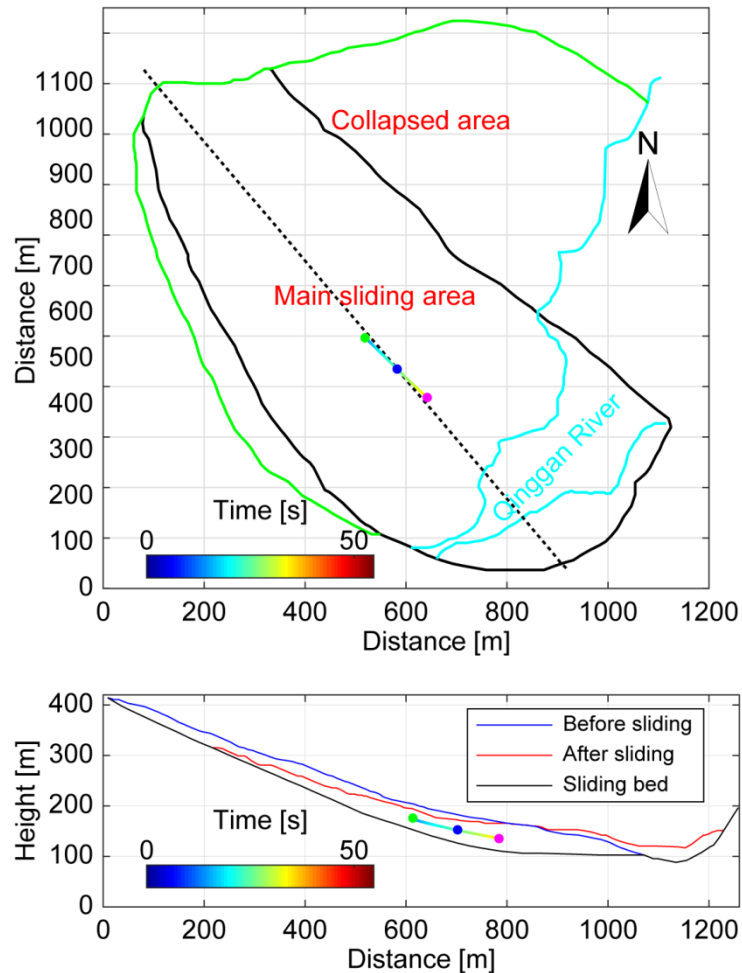
69 Based on the inverted landslide force histories, relationships between the
70 maximum inverted forces and sliding volumes can be derived and such relationships
71 can be used to estimate sliding volumes in future landslide studies [*Chao et al., 2016;*
72 *Ekström and Stark, 2013*]. Landslide basal frictions are either estimated directly by
73 adopting a block model [e.g., *Allstadt, 2013; Brodsky et al., 2003; Yamada et al., 2013;*
74 *Zhao et al., 2015*] or obtained from a joint analysis with numerical landslide
75 simulations [*Moretti et al., 2015; Moretti et al., 2012; Yamada et al., 2016; Yamada et*
76 *al., 2018*]. An important precondition for the above interpretation work is that the
77 inverted landslide force histories are reasonable approximations. However, at least
78 two important factors that affect the quality of the interpretation work are rarely
79 discussed in previous studies. The first one is how to choose a proper frequency band
80 to carry out the force-history inversion; and the second one is how mass entrainments
81 during sliding affect the estimated parameters during interpretation.

82 In this paper, we first discuss how to estimate the accuracy of the inverted
83 force histories and then propose an approach to determine the proper frequency band
84 used in the inversion in order to rebuild landslide movement parameters from inverted
85 force histories. We demonstrate our approach using the Qianjiangping landslide that
86 occurred in 2003. Using the force history obtained by inverting long-period seismic
87 waveform data, we build a model to study the effects of the portion of the initial
88 sliding mass and the location of the mass entrainment on the estimated mass and other
89 interpretation parameters.

90 2. The Qianjiangping Landslide and Seismic Observations

91 The catastrophic Qianjiangping landslide occurred at approximately 16:20:00
92 UT on July 13, 2003. It had a volume of about $2.04 \times 10^7 \text{ m}^3$ and caused substantial
93 economic loss. It was located on the left bank of the Qinggan River within the Three
94 Gorges Reservoir area. The river bends in front of the Qianjiangping slope and the
95 erosion at the toe of the slope caused by the river is believed to have had a negative
96 impact on the slope stability. As shown in Figure 1, the landslide had a tongue-like
97 shape in map view, with a length of $\sim 1,200$ m and a width of $\sim 1,000$ m. It moved

98 ~250 m in the main sliding direction of S45°E [Wang *et al.*, 2008]. The Qianjiangping
 99 landslide consisted of a main sliding area and a collapsed area. The toe of the main
 100 sliding area slid into the Qinggan River, blocking the flow. On the contrary, the
 101 collapsed area was just drawn down by the movement of the main sliding area with a
 102 very limited sliding distance [Wang *et al.*, 2008].



103

104 **Figure 1.** Map (upper panel) and central longitudinal section (lower panel) of the
 105 Qianjiangping landslide (adapted from [Wang *et al.*, 2008]).
 106

107 We collected seismic records for this landslide event at seismic stations within
 108 an epicentral distance of ~10 degrees. The locations of the seismic stations are shown
 109 in Figure S1. The nearest seismic station was ENH with an epicentral distance of
 110 ~131.6 km. Figure S2 shows the East-West component seismic records at the ENH
 111 station within different frequency bands. The start time of the low-frequency
 112 waveform associated with the landslide event is much earlier than that of the
 113 high-frequency waveform. High-frequency seismic signals appeared close to the end
 114 of the event. With the appearance of the high-frequency seismic signal, there appeared
 115 a short-duration, energetic pulse on the low-frequency waveform.

116 Since high frequency energy decays rapidly with distance, it was only detected

117 by the nearest two seismic stations. On the other hand, low-frequency seismic energy
118 could be detected by seismic station as far as ~1000 km (Figure S3). Seismic
119 recordings at three coastal stations, SSE, KMNB, and MATB, had relatively poor
120 signal-to-noise ratios. Recordings at MATB were too noisy and were not plotted in
121 Figure S3. Recordings at SSE had very small amplitudes. The arrival times at SSE
122 and KMNB were ~70 seconds later than those at other stations of similar epicentral
123 distances, which is likely due to differences in seismic velocities along different
124 source-station paths.

125

126 **3. Landslide Force History Inversion**

127 A robust force-history inversion should at least meet two levels of
128 requirements. First, the entire inversion workflow, consisting of seismic data
129 processing, calculation of the Green's functions, the implementation of the solution
130 algorithm, should be mathematically correct. A typical sign of reaching this level of
131 requirement is a reasonable match between the recorded seismic waveforms and the
132 corresponding synthetic waveforms, sometimes quantified using certain
133 goodness-of-fit measurements. At the current stage, the majority of force-history
134 inversion studies can meet this level of requirements.

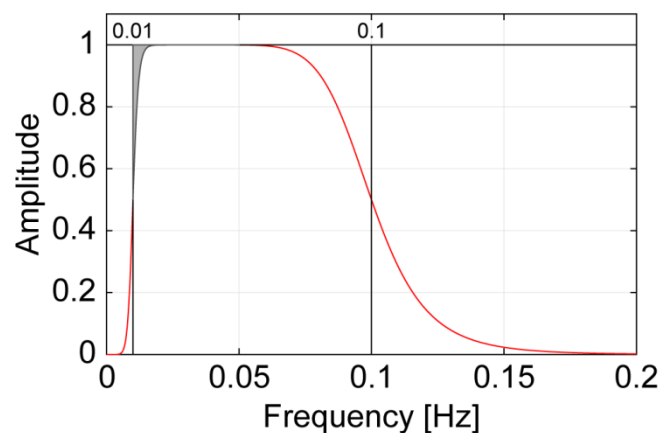
135 The second level of requirements is associated with physical feasibilities, i.e.,
136 the dynamic and kinematic parameters inferred from the inverted force histories
137 should be within reasonable ranges given by the physical processes of the landslide.
138 For example, inferred sliding trajectories should be generally consistent with actual
139 sliding traces of the mass center. The frequency band of the seismic data used in the
140 inversion can have a substantial impact. For example, force histories of the Bingham
141 Canyon Mine landslides inverted using seismic data within different frequency bands
142 had nonnegligible differences not only in amplitudes but also in the shape and the
143 duration [Hibert *et al.*, 2014; Moore *et al.*, 2017; Zhang *et al.*, 2020]. It is unlikely
144 that all of the inverted force histories were physically feasible.

145 It has been recognized that the long-period seismic signals used in landslide
146 force history inversions are generated by unloading and reloading of the solid earth
147 while the sliding mass accelerates and decelerates [e.g., Chao *et al.*, 2016; Ekström
148 and Stark, 2013; Hibert *et al.*, 2014; Hibert *et al.*, 2015]. Therefore, to rebuild the
149 acceleration/deceleration history of a sliding mass, the seismic waveform data used in
150 the inversion must have a duration that fully covers the duration of the
151 acceleration/deceleration process. Specifically, if the longest duration of the
152 acceleration/deceleration processes is T , the lowest frequency of the seismic
153 waveform data should be no larger than $1/2T$ Hz. Normally, a landslide contains one
154 major acceleration phase and one major deceleration phase. In practice we estimate
155 the low frequency bound of the passing band using the whole duration of the sliding
156 event by assuming the same duration of the acceleration and deceleration phases.

157 In practice, we usually do not know the duration of the sliding event prior to
158 the force-history inversion. However, the duration of the low-pass filtered seismic

159 waveforms at the nearest seismic station provides a reasonable approximation of the
160 duration of the sliding event. For the Qianjiangping landslide, the waveform at the
161 nearest station (Figure S3) shows that the duration of the sliding event was ~66 s. We
162 therefore set the lower bound of the frequency band used in our landslide force history
163 inversion at 0.015 Hz. Seismic signals below this lower frequency bound should be
164 removed thorough filtering since they are unrelated to the sliding event and may
165 contaminate the force-history inversion results. It should be noted that commonly
166 used filters usually have transition bands around corner frequencies, which can
167 potentially distort the signals in the passing band. An example of the amplitude
168 response of a 4th-order 0.01 – 0.1 Hz Butterworth band-pass filter is shown in Figure 2.
169 Signals between the low-frequency bound and the corner frequency (shaded area in
170 Figure 2), is distorted. For the Xinmo landslide, this distortion may explain why *Z-y*
171 *Li et al.* [2019] can rebuild a reasonable sliding trajectory, while the trajectory of *W Li*
172 *et al.* [2019] shows a circle-back, even though both studies used the same
173 low-frequency bound in seismic data processing.

174 The high-frequency bound should be determined by considering two factors:
175 small-scale features in the landslide source that we would like to resolve and
176 heterogeneities in elastic media along source-station paths that we can account for in
177 the Green's functions. Errors in the inverted force histories due to high-frequency
178 seismic noises are usually concentrated in high-frequency bands and their influences
179 on the reconstruction of the sliding trajectories through integration over time are
180 usually negligible. However, they may lead to misidentification or mischaracterization
181 of small-scale landslide mass movements. In our study of the Qianjiangping landslide,
182 we used a flat-layered velocity model derived from [Crust 1.0](#) and the Green's
183 functions were computed using the matrix propagation method of *Wang* [1999]. The
184 velocity model and the resulting Green's functions are accurate below 0.1 Hz for
185 stations within ~500 km epicentral distance (i.e., station ENH and XAN). Therefore,
186 the high-frequency bound of our band-pass filter was set to 0.1 Hz. The band-pass
187 filtered seismic waveforms were then used in our inversion, which was carried out in
188 the frequency domain to improve computational efficiency.



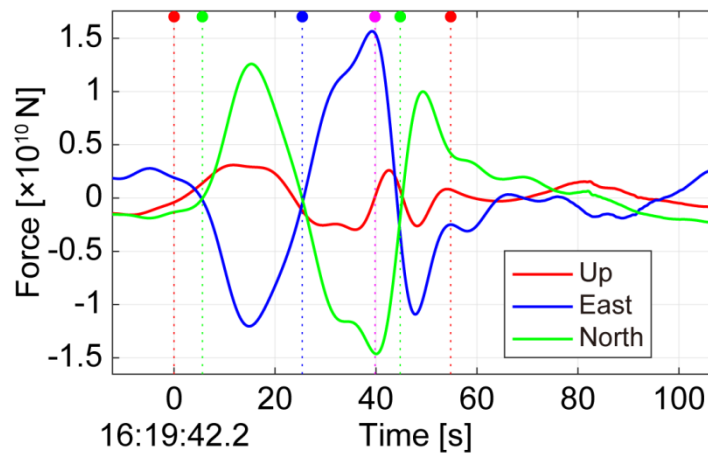
189
190
191

Figure 2. Amplitude response of a non-causal fourth-order 0.01 – 0.1 Hz Butterworth bandpass filter.

192

193 In general, synthetic waveforms computed from the inverted force histories
194 show excellent fit with the corresponding observed waveforms (Figure S4),
195 suggesting that our inversion result likely meets the first level of requirement. From
196 the inverted landslide force history shown in Figure 3, we recognize that the landslide
197 started at $\sim 16:19:42.2$ with a duration of ~ 54.8 s. The maximum absolute force
198 reached $\sim 2.1 \times 10^{10}$ N. When determining the start and end times for a landslide, we
199 usually choose the times closest to zero forces, such as those denoted using green
200 dashed lines in Figure 3. We call them *apparent* start and end times. However, if we
201 carefully observe the force curves, it might be more reasonable to define an earlier
202 start time and a later end time as denoted using red dashed lines in Figure 3. We call
203 them *real* start and end times. Force curves show an overall deviation from zero
204 before the real start time and slow energy decay after the real end time. We believe
205 this phenomenon is caused by filtering. Seismic waveform data are commonly filtered
206 using a non-causal band-pass filter before being used in the inversion, which is
207 equivalent to apply the same filter to the inverted force history. The filtering operation
208 could potentially modify the shape of the inverted force history by shifting values of
209 the start and end times from the baseline.

210



211

212 **Figure 3.** Inverted force history for the Qianjiangping landslide. Red dashed lines,
213 green dashed lines, the blue dashed line, and the magenta dashed line denote the real
214 start and end times, apparent start and end times, the maximum velocity time, and the
215 maximum displacement time, respectively.

216

217 4. Landslide dynamics

218 Based on Newton's third law of motion, the forces acting on the sliding mass
219 can be obtained by multiplying the inverted force history by -1 [e.g., *Gualtieri and*
220 *Ekström, 2018; Kanamori and Given, 1982; Yamada et al., 2013*]. We can then use
221 this force to either calculate velocity and displacement distributions of the sliding

222 material for a given mass [e.g., *W Li et al.*, 2019; *Z-y Li et al.*, 2019; *Yu et al.*, 2020]
223 or estimate the sliding mass by minimizing the discrepancies with the sliding
224 trajectories from satellite images [e.g., *Hibert et al.*, 2014]. We adopted the second
225 approach and estimated the sliding mass to be $\sim 2.1655 \times 10^{10}$ kg by minimizing the
226 discrepancies with the trajectories of the sliding material weight center from *Wang et al.*
227 *al.* [2008], which is shown in Figure 1. Both the recovered horizontal and vertical
228 trajectories fit well with the observations.

229 We further estimated the displacement and velocity distributions along time
230 and obtained the maximum movement speed of 9.4 m/s as shown in Figure S5d. We
231 aligned the East-West component seismic records at the ENH station with the origin
232 time of the landslide by assuming a seismic wave propagation velocity of 3.35 km/s.
233 The original broadband seismogram, 1 Hz high-pass filtered seismogram and 0.1 Hz
234 low-pass filtered seismograms are shown in Figure S5a, b, and c, respectively. It
235 could be observed that the long period seismic energy that is used in the landslide
236 force history inversion fits almost perfectly with the landslide start time estimated
237 from the inverted force history; however, it is hardly visible to the naked eye in the
238 original broadband seismogram. High-frequency signal did not show up immediately
239 after the occurrence of the event; instead, a small amplitude high-frequency
240 wave-train appeared after the maximum velocity and a large amplitude
241 high-frequency wave-train appeared very close to the end of the event, suggesting that
242 the process generating the high-frequency seismic signals was not directly related to
243 the main landslide movement. It should be noted that the arrival time of the
244 high-frequency signals is not necessarily the occurrence time of the process
245 generating the high-frequency signals since we assumed a seismic wave propagation
246 velocity of 3.35 km/s to align the seismic records. The actual velocity of the
247 high-frequency waves could be larger than our assumption, which could potentially
248 make the arrival time earlier than the occurrence time of the process generating the
249 high-frequency signals.

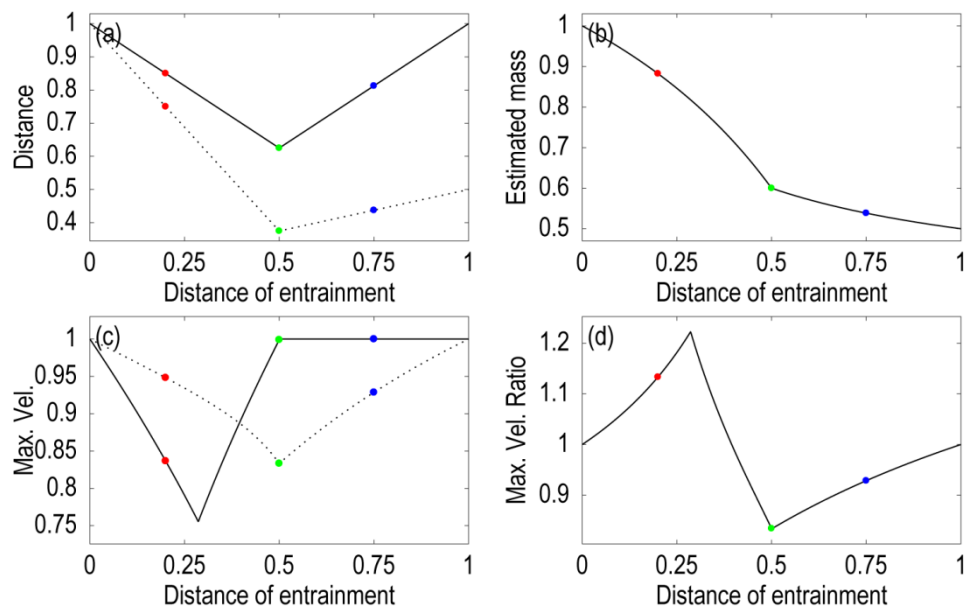
250

251 5. Discussion

252 The estimated mass for the Qianjiangping landslide is $\sim 2.1655 \times 10^{10}$ kg, which
253 gives a sliding volume of $\sim 1.08 \times 10^7$ m³, if we assume a density of 2.0×10^3 kg/m³. The
254 estimated volume is $\sim 54.14\%$ of that obtained from the field survey [*Wang et al.*,
255 2008]. We can explain the mass discrepancy by analyzing the influence of mass
256 mobilization and entrainment during sliding using a simple model. Figure S6a shows
257 the shape of a simple slope, which results in constant accelerations for speed-up and
258 slow-down phases as shown in Figure S6b. In realistic situations, mass mobilizations
259 and entrainments occur very fast and the mobilized mass speed up to and the sliding
260 mass slow down to an equivalent velocity during the process. To simplify calculation,
261 we assume this process is instantaneous. In the model, 50% of the mass is from initial
262 sliding and the other 50% is from mobilization and entrainment during sliding. We put
263 the entrained mass at different locations from the beginning to the end to derive their

264 force and velocity distributions along the runout distance and evaluate their effects on
 265 the estimation of the sliding mass. In Figure S6, we use red, green, and blue dashed
 266 lines and solid circles to represent the estimated parameters when the entrained mass
 267 is located at runout distances of 0.2, 0.5, and 0.75, respectively.

268 We use the forces, which could be approximated using the inverted forces, and
 269 runout distances to estimate the sliding mass for each entrainment location. We first
 270 integrate the forces twice with respect to time and obtain their maximum values,
 271 which are shown as the dashed line in Figure 4a, and then divide them by runout
 272 distances, shown as the solid line in Figure 4a. From the estimated sliding mass
 273 shown in Figure 4b, it could be observed that if there was a mass entrainment event,
 274 wherever its location, the estimated mass would be smaller than the total mass. If the
 275 entrainment occurred at the slow-down stage (i.e., runout distance larger than 0.5),
 276 which frequently happens in reality, the estimated mass is no more than 60% of the
 277 total mass. We can use the estimated mass to derive velocity distributions and their
 278 maximum values and the estimated maximum velocities are 83.38% - 122.26% of
 279 actual maximum velocities as shown in Figure 4d.



280

281 **Figure 4.** (a) real runout distances (solid line) and the maximum values of the
 282 integrations of the forces twice with respect to time (dashed line); (b) estimated mass
 283 for different entrainment location; (c) real (solid line) and estimated (dashed line)
 284 maximum velocities; (4) the ratio of the estimated maximum velocities to the real
 285 maximum velocities.

286

287 The above model calculations show that when the entrainment occurs in the
 288 slow-down phase, the estimated mass is far less than the total mass and is a closer
 289 approximation to the initial sliding mass. The forces in the slow-down phase show
 290 large amplitudes and short durations, which is in contrary to the predications of the
 291 sliding block model [Zhao *et al.*, 2015]. The inverted landslide force history for the

292 Xinmo landslide shows a shorter duration and larger amplitudes in the slow-down
293 phase as compared with the force in the speed-up phase [Z-y Li *et al.*, 2019],
294 suggesting that the landslide mobilized and entrained a large amount of pre-existing
295 deposits during the slow-down phase, which is supported by field surveys [Fan *et al.*,
296 2017]. In addition, Z-y Li *et al.* [2019] estimated the Xinmo landslide trajectories
297 using only the initial sliding volume of 4.46 million m³, accounting for only ~34% of
298 the total deposits (13 million m³ [Fan *et al.*, 2017]), which is also consistent with the
299 model calculations.

300 Seismically inferred total masses of two glacier collapses in western Tibet by
301 Käüb *et al.* [2018] were underestimated by a factor of about 3-6 compared with the
302 avalanche deposit volumes inferred from satellite images. The authors attributed this
303 discrepancy to a significant decrease in mass before bulk material arrest due to
304 progressive ice deposition along the path. However, an alternative explanation could
305 be that the initial sliding mass was small and it mobilized and entrained a large
306 amount of material during the slow-down phase. If the initial sliding mass was large,
307 large forces in the initial stage should have been detected through the inversion. Mass
308 mobilization and entrainment slow down the entire movement velocity; however,
309 small slope angles and basal friction coefficients in the slow-down stage result in
310 almost undetectable resistant forces, which lead to long runout distances. It could be
311 inferred from the model calculations that the derived empirical relations between
312 maximum inverted forces and sliding volumes may have systematic uncertainties,
313 since the inverted force has a stronger relation with the initial sliding mass than the
314 total deposit mass. Similarly, studies on landslide basal frictions based on landslide
315 force inversion should carefully consider the influence of mass variations during
316 sliding.

317 For the Qianjiangping landslide, field survey showed that the collapsed area
318 was drawn down by the movement of the main sliding area and its sliding distance
319 was very limited, suggesting that this part of mass did not participate in generating the
320 seismically detected forces. This might be an explanation for the mass discrepancy. To
321 find out when the draw-down occurred, we analyzed the high frequency seismic
322 signals that occurred very close to the end of the landslide event. The East-West
323 component broadband record at the ENH station, its S-transform [Stockwell, 2007;
324 Stockwell *et al.*, 1996] spectrogram and the 1 Hz high-pass filtered record are shown
325 in Figure S7. Since the amplitude in the later section is substantially larger than that in
326 the earlier section, spectrograms of such signals are usually dominated by the large
327 amplitude signals. We therefore normalized each time component of the spectrogram
328 [Huang *et al.*, 2017]. The first part of the signal shows small amplitude with higher
329 frequency, while the second part shows large amplitude with lower frequency and
330 obvious wave dispersion, suggesting that they are body waves and surface waves
331 produced by a rupture. With the help of the spectrogram and the high-pass filtered
332 seismic record we estimated the times of the p phase, s phase, and surface-wave phase
333 were 16:20:48.4, 16:21:4.2, and 16:21:7.2, respectively. The dominant frequency of
334 the body waves was about 2 Hz, which is substantially lower than that of typical small
335 earthquakes. The low frequencies of both body waves and surface wave signals and

336 the well-developed surface wave suggest that the rupture occurred on the earth surface.
337 We estimated the epicentral distance and the occurrence time of the event to be 134.18
338 km and 16:20:26.4 assuming the P-wave velocity and S-wave velocity of 6.1 km/s
339 and 3.55 km/s, respectively, suggesting that the event was a rupture on the earth
340 surface during the landslide. We conjecture that the high-frequency seismic signal was
341 generated when the draw-down occurred. The main sliding area mobilized the
342 collapsed area shortly before it stopped, generating the high frequency seismic signal.
343 And then, both of them stopped shortly after, resulting in a limited sliding distance of
344 the collapsed area. Therefore, the estimated mass could be an approximation of the
345 sliding mass in the main sliding area, which is smaller than total deposits.

346

347 **6. Conclusions**

348 A reasonable landslide force history inversion using long-period seismic
349 records should meet two levels of requirements, i.e., mathematically correct and
350 physically consistent. To obtain a physically consistent inversion result, the low
351 frequency bound of the passband used in seismic data processing should have a period
352 that is longer than the landslide duration. We propose an approach to determine the
353 frequency band required by the inversion to reliably reconstruct landslide movement
354 parameters from force-history inversion results. Based on the landslide force history
355 inversion from long-period seismic waveform for the 2003 Qianjiangping landslide,
356 we propose a simple model to study the effects of the initial sliding mass and the
357 location of the mass entrainment on the seismically estimated sliding mass and other
358 parameters. We conclude that if there is a mass entrainment, the seismically estimated
359 mass is smaller than the total mass and if the entrainment occurs at the slow-down
360 phase the seismically estimated mass is a closer approximation of the initial sliding
361 mass.

362 **Acknowledgements, Samples, and Data**

363 The seismic data used in this study are from IRIS (<https://www.iris.edu/hq/>).
364 The velocity model used in the inversion is derived from Crust1.0
365 (<https://igppweb.ucsd.edu/~gabi/crust1.html>). SAC software packages
366 (<http://ds.iris.edu/files/sac-manual/>) were used for the seismic data processing.
367 QSEIS06 (<https://www.gfz-potsdam.de/>) was used to calculate Green's Functions.
368 This work was completed when the corresponding author was a visiting scholar at the
369 University of Wyoming, which was financially supported by the China Scholarship
370 Council under Grant 201904190026.

371 **References**

372 Allstadt, K. (2013), Extracting source characteristics and dynamics of the August
373 2010 Mount Meager landslide from broadband seismograms, *J. Geophys. Res. Earth*
374 *Surf.*, *118*(3), 1472-1490, doi: 10.1002/jgrf.20110.
375 Brodsky, E. E., E. Gordeev, and H. Kanamori (2003), Landslide basal friction as

376 measured by seismic waves, *Geophys. Res. Lett.*, 30(24), 2236, doi:
377 10.1029/2003GL018485.

378 Chao, W.-A., L. Zhao, S.-C. Chen, Y.-M. Wu, C.-H. Chen, and H.-H. Huang (2016),
379 Seismology-based early identification of dam-formation landslide events, *Sci. Rep.*,
380 6, 19259, doi: 10.1038/srep19259.

381 Dahlen, F. A. (1993), Single-force representation of shallow landslide sources, *Bull.*
382 *Seismol. Soc. Am.*, 83(1), 130-143.

383 Ekström, G., and C. P. Stark (2013), Simple scaling of catastrophic landslide
384 dynamics, *Science*, 339(6126), 1416-1419, doi: 10.1126/science.1232887.

385 Fan, X., Q. Xu, G. Scaringi, L. Dai, W. Li, X. Dong, X. Zhu, X. Pei, K. Dai, and H.-B.
386 Havenith (2017), Failure mechanism and kinematics of the deadly June 24th 2017
387 Xinmo landslide, Maoxian, Sichuan, China, *Landslides*, 14(6), 2129-2146, doi:
388 10.1007/s10346-017-0907-7.

389 Fukao, Y. (1995), Single-force representation of earthquakes due to landslides or the
390 collapse of caverns, *Geophys. J. Int.*, 122(1), 243-248, doi:
391 10.1111/j.1365-246X.1995.tb03551.x.

392 Gualtieri, L., and G. Ekström (2018), Broad-band seismic analysis and modeling of
393 the 2015 Taan Fjord, Alaska landslide using Instaseis, *Geophys. J. Int.*, 213(3),
394 1912-1923, doi: 10.1093/gji/ggy086.

395 Hasegawa, H., and H. Kanamori (1987), Source mechanism of the magnitude 7.2
396 Grand Banks earthquake of November 1929: Double couple or submarine landslide?,
397 *Bull. Seismol. Soc. Am.*, 77(6), 1984-2004.

398 Hibert, C., G. Ekström, and C. P. Stark (2014), Dynamics of the Bingham Canyon
399 Mine landslides from seismic signal analysis, *Geophys. Res. Lett.*, 41(13), 4535-4541,
400 doi: 10.1002/2014GL060592.

401 Hibert, C., C. Stark, and G. Ekström (2015), Dynamics of the Oso-Steelhead landslide
402 from broadband seismic analysis, *Nat. Hazards Earth Syst. Sci.*, 15(6), 1265-1273, doi:
403 10.5194/nhess-15-1265-2015.

404 Huang, X., Z. Li, D. Yu, Q. Xu, J. Fan, Z. Hao, and Y. Niu (2017), Evolution of a
405 giant debris flow in the transitional mountainous region between the Tibetan Plateau
406 and the Qinling Mountain range, Western China: Constraints from broadband seismic
407 records, *J. Asian Earth Sci.*, 148, 181-191, doi: 10.1016/j.jseaes.2017.08.031.

408 Kääb, A., et al. (2018), Massive collapse of two glaciers in western Tibet in 2016 after
409 surge-like instability, *Nat. Geosci.*, 11(2), 114-120, doi: 10.1038/s41561-017-0039-7.

410 Kanamori, H., and J. W. Given (1982), Analysis of long - period seismic waves
411 excited by the May 18, 1980, eruption of Mount St. Helens—A terrestrial monopole?,
412 *J. Geophys. Res. Solid Earth*, 87(B7), 5422-5432, doi: 10.1029/JB087iB07p05422.

413 Kanamori, H., J. W. Given, and T. Lay (1984), Analysis of seismic body waves
414 excited by the Mount St. Helens eruption of May 18, 1980, *J. Geophys. Res. Solid*

415 *Earth*, 89(B3), 1856-1866, doi: 10.1029/JB089iB03p01856.

416 Li, W., Y. Chen, F. Liu, H. Yang, J. Liu, and B. Fu (2019), Chain-Style Landslide
417 Hazardous Process: Constraints From Seismic Signals Analysis of the 2017 Xinmo
418 Landslide, SW China, *J. Geophys. Res. Solid Earth*, 124, 2025-2037, doi:
419 10.1029/2018JB016433.

420 Li, Z.-y., X.-h. Huang, D. Yu, J.-r. Su, and Q. Xu (2019), Broadband-seismic analysis
421 of a massive landslide in southwestern China: Dynamics and fragmentation
422 implications, *Geomorphology*, 336, 31-39, doi: 10.1016/j.geomorph.2019.03.024.

423 Li, Z., X. Huang, Q. Xu, D. Yu, J. Fan, and X. Qiao (2017), Dynamics of the Wulong
424 landslide revealed by broadband seismic records, *Earth Planets Space*, 69(1), 27, doi:
425 10.1186/s40623-017-0610-x.

426 Moore, J. R., K. L. Pankow, S. R. Ford, K. D. Koper, J. M. Hale, J. Aaron, and C. F.
427 Larsen (2017), Dynamics of the Bingham Canyon rock avalanches (Utah, USA)
428 resolved from topographic, seismic, and infrasound data, *J. Geophys. Res. Earth Surf.*,
429 122(3), 615-640, doi: 10.1002/2016JF004036.

430 Moretti, L., K. Allstadt, A. Mangeney, Y. Capdeville, E. Stutzmann, and F. Bouchut
431 (2015), Numerical modeling of the Mount Meager landslide constrained by its force
432 history derived from seismic data, *J. Geophys. Res. Solid Earth*, 120(4), 2579-2599,
433 doi: 10.1002/2014JB011426.

434 Moretti, L., A. Mangeney, Y. Capdeville, E. Stutzmann, C. Huggel, D. Schneider, and
435 F. Bouchut (2012), Numerical modeling of the Mount Steller landslide flow history
436 and of the generated long period seismic waves, *Geophys. Res. Lett.*, 39(16), L16402,
437 doi: 10.1029/2012GL052511.

438 Sheng, M., R. Chu, Y. Wang, and Q. Wang (2020), Inversion of Source Mechanisms
439 for Single - Force Events Using Broadband Waveforms, *Seismol. Res. Lett.*, 91(3),
440 1820-1830, doi: 10.1785/0220190349.

441 Stockwell, R. G. (2007), A basis for efficient representation of the S-transform,
442 *Digital Signal Processing*, 17(1), 371-393, doi: 10.1016/j.dsp.2006.04.006.

443 Stockwell, R. G., L. Mansinha, and R. Lowe (1996), Localization of the complex
444 spectrum: the S transform, *IEEE Trans. on Signal Processing*, 44(4), 998-1001, doi:
445 10.1109/78.492555.

446 Wang, F., Y. Zhang, Z. Huo, X. Peng, S. Wang, and S. Yamasaki (2008), Mechanism
447 for the rapid motion of the Qianjiangping landslide during reactivation by the first
448 impoundment of the Three Gorges Dam reservoir, China, *Landslides*, 5(4), 379-386,
449 doi: 10.1007/s10346-008-0130-7.

450 Wang, R. (1999), A simple orthonormalization method for stable and efficient
451 computation of Green's functions, *Bull. Seismol. Soc. Am.*, 89(3), 733-741.

452 Yamada, M., H. Kumagai, Y. Matsushi, and T. Matsuzawa (2013), Dynamic landslide
453 processes revealed by broadband seismic records, *Geophys. Res. Lett.*, 40(12),
454 2998-3002, doi: 10.1002/grl.50437.

455 Yamada, M., A. Mangeney, Y. Matsushi, and L. Moretti (2016), Estimation of
456 dynamic friction of the Akatani landslide from seismic waveform inversion and
457 numerical simulation, *Geophys. J. Int.*, 206(3), 1479-1486, doi: 10.1093/gji/ggw216.

458 Yamada, M., A. Mangeney, Y. Matsushi, and T. Matsuzawa (2018), Estimation of
459 dynamic friction and movement history of large landslides, *Landslides*, 15(10),
460 1963-1974, doi: 10.1007/s10346-018-1002-4.

461 Yu, D., X. Huang, and Z. Li (2020), Variation patterns of landslide basal friction
462 revealed from long-period seismic waveform inversion, *Nat. Hazards*, 100(1),
463 313-327, doi: 10.1007/s11069-019-03813-y.

464 Zhang, Z., S. He, and Q. Li (2020), Analyzing high-frequency seismic signals
465 generated during a landslide using source discrepancies between two landslides,
466 *Engineering Geology*, 272, 105640, doi: 10.1016/j.enggeo.2020.105640.

467 Zhao, J., C. J. Ouyang, S. D. Ni, R. S. Chu, and A. Mangeney (2020), Analysis of the
468 2017 June Maoxian landslide processes with force histories from seismological
469 inversion and terrain features, *Geophys. J. Int.*, 222(3), 1965-1976, doi:
470 10.1093/gji/ggaa269.

471 Zhao, J., et al. (2015), Model space exploration for determining landslide source
472 history from long-period seismic data, *Pure Appl. Geophys.*, 172(2), 389-413, doi:
473 10.1007/s00024-014-0852-5.

474

1
2
3
4
5
6
7
8
9
10
11
12
13
14
15
16
17
18
19
20
21
22

Geophysical Research Letters

Supporting Information for

On rebuilding landslide parameters from long-period seismic waveform inversion

Xiao Wang¹, Xinghui Huang^{1,2*}, Po Chen², Lei Xu³, Heng Wang⁴, Wenze Deng¹, Dan Yu¹,
Zhengyuan Li¹, Qiang Xu⁵

¹China Earthquake Networks Center, Beijing, China

²Department of Geology and Geophysics, University of Wyoming, Laramie, United States

³The 7th Institute of Geology & Mineral Exploration of Shandong Province, Linyi, China

⁴Center for Economic Geology Research, University of Wyoming, Laramie, Wyoming, United States

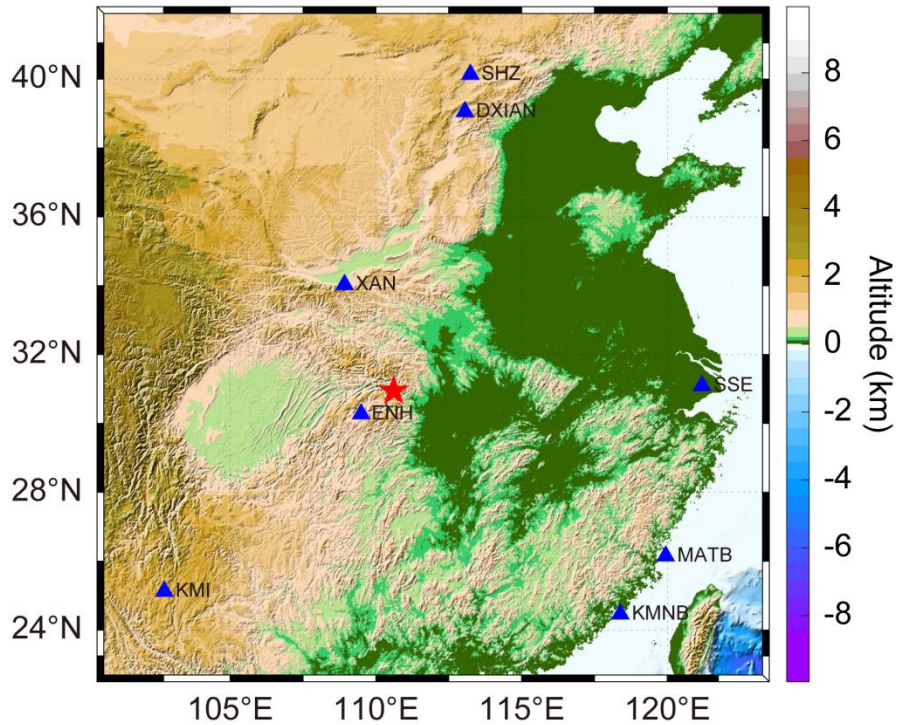
⁵State Key Laboratory of Geohazard Prevention and Geoenvironment Protection, Chengdu University of
Technology, Chengdu, China

Contents of this file

Figures S1 to S7

Introduction

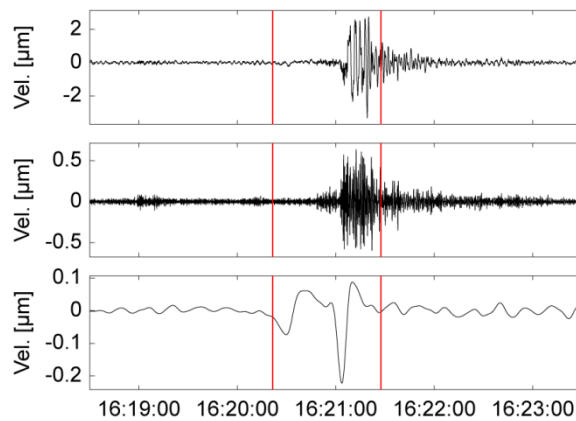
This supporting information provides seven additional figures.



23

24 **Figure S1.** Location of seismic stations used in the study (blue triangles) and the landslide (red
 25 star).

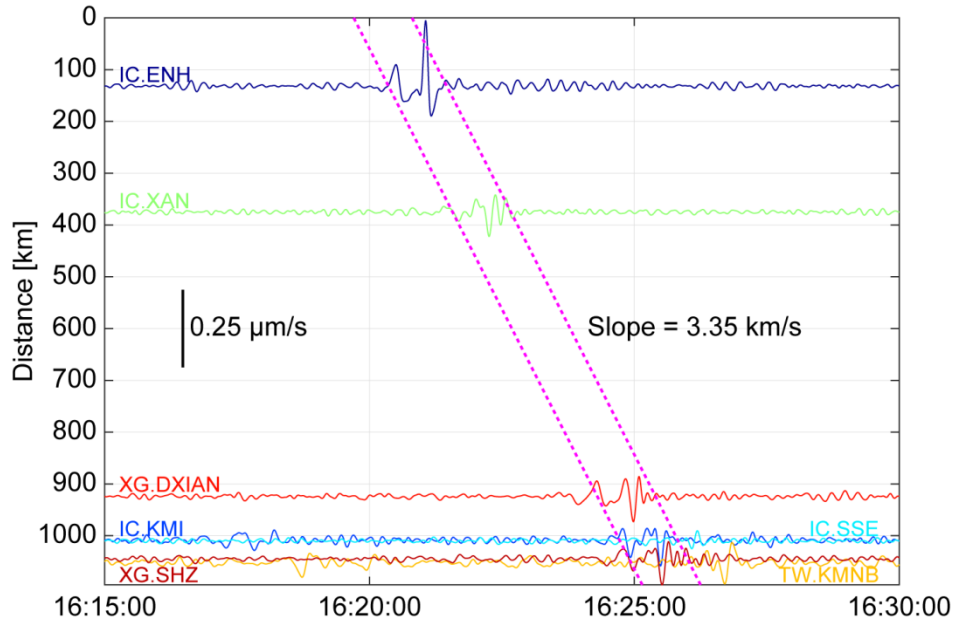
26



27

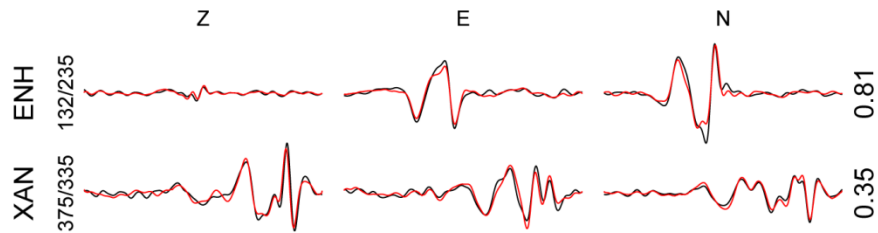
28 **Figure S2.** Broadband seismic records for the Qianjiangping landslide at the ENH seismic
 29 station. Original record, high-pass filtered record at 1 Hz, and low-pass filtered record at 0.1 Hz
 30 are provided from top to bottom. Red vertical lines show start and end times of the event
 31 recognized from low-pass filtered seismic records.

32



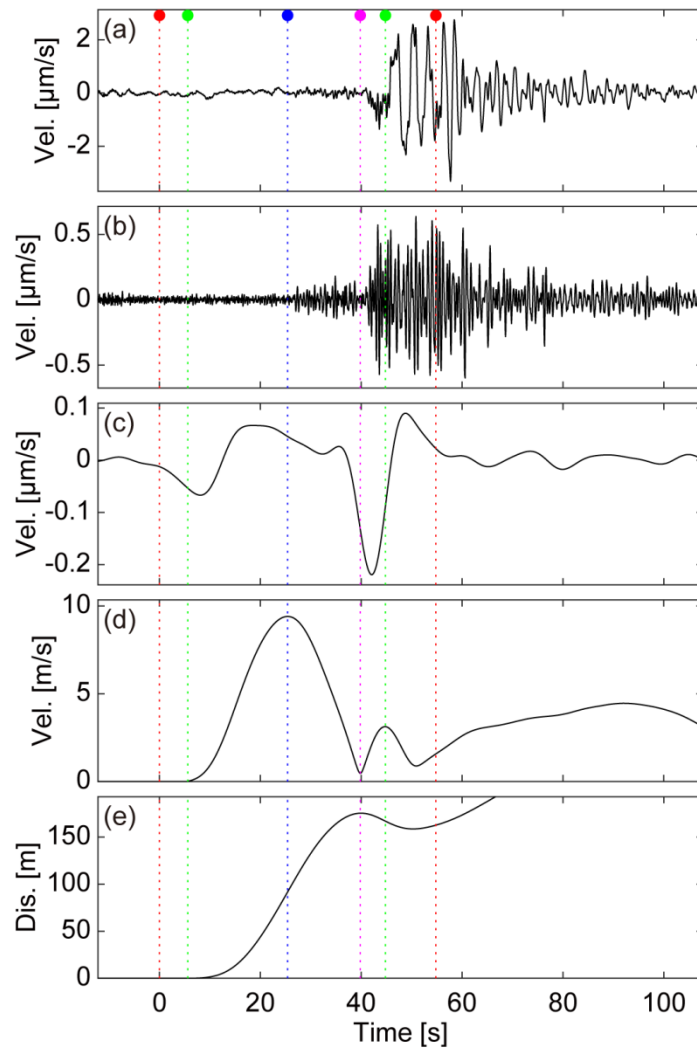
33
34
35
36
37
38

Figure S3. Seismograms recorded at seismic stations in the surrounding area of the landslide and filtered using a frequency band of 0.01 – 0.1 Hz. The magenta dashed lines give the start and end times of the event on seismograms. The propagation velocity is estimated to be 3.35 km/s.



39
40
41
42
43

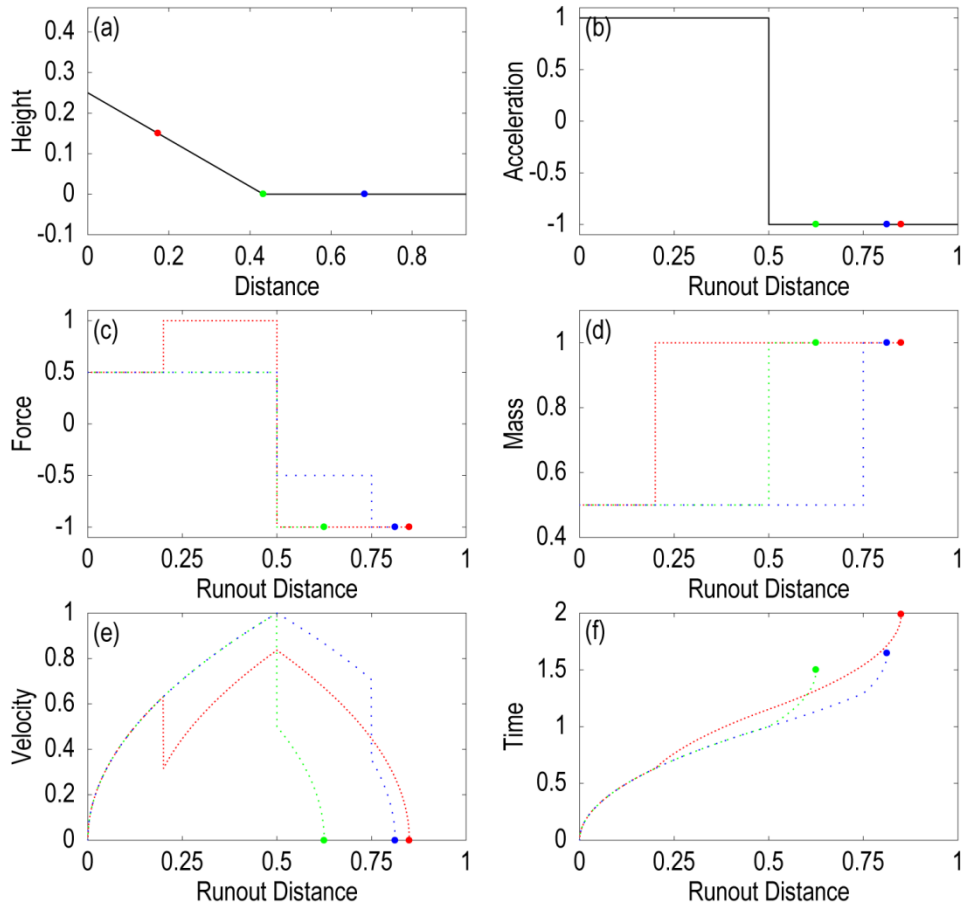
Figure S4. Recorded (black lines) and synthetic (red lines) seismic waveforms. Station name and distance (km)/azimuth (degree) are given at the left of each trace. The maximum amplitude of the three components is given in μm to the right of the traces.



44

45 **Figure S5.** (a) East-West component seismic record of the ENH station, the nearest station
 46 from the landslide; (b) 1 Hz high-pass filtered seismic record; (c) 0.1 Hz low pass filtered seismic
 47 record. Estimation of absolute velocity (d) and displacement (e) of the sliding mass from
 48 inverted landslide force history.

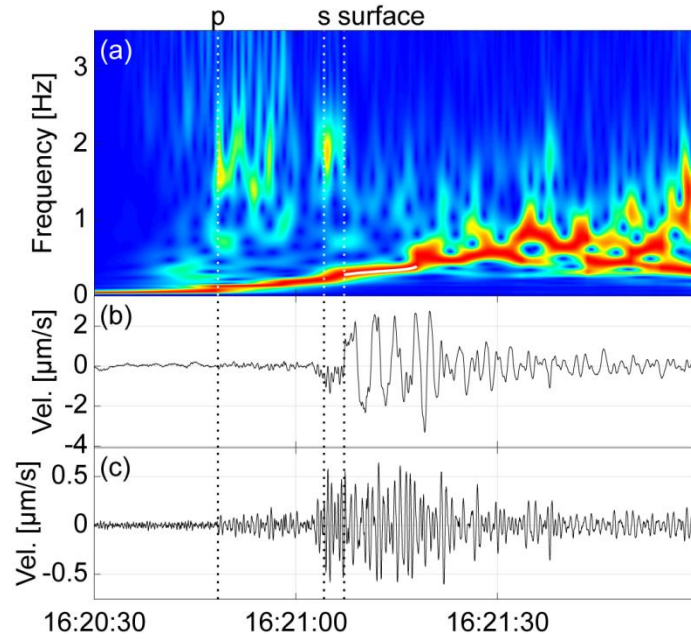
49



50

51 **Figure S6.** (a) the schematic map of the slope model; (b) accelerations for speed-up and slow-
 52 down phases; (c) force, (d) mass, (e) velocity, and (f) time distributions along runout distance
 53 when the entrained mass is put at runout distances of 0.2, 0.5, and 0.75, respectively, denoted
 54 using red, green, and blue dashed lines and solid circles.

55



56

57 **Figure S7.** (a) Time-by-time normalized S-Transform spectrogram for the East-West
58 component seismic record at the ENH station; (b) the East-West component seismic record at
59 the ENH station; (c) 1 Hz high-pass filtered seismic record.